Phosphorus slags

Structural insights, dissolution behavior, and potential as sustainable supplementary cementitious materials

Zhang, Yu; Nie, Shuai; Liu, Chen

DOI
10.1016/j.cej.2025.160463

Publication date
2025

Document Version
Final published version

Published in
Chemical Engineering Journal

Citation (APA)
Zhang, Y., Nie, S., & Liu, C. (2025). Phosphorus slags: Structural insights, dissolution behavior, and potential as sustainable supplementary cementitious materials. *Chemical Engineering Journal*, *507*, Article 160463. https://doi.org/10.1016/j.cej.2025.160463

Chemical Engineering Journal 507 (2025) 160463

Contents lists available at ScienceDirect

Chemical Engineering Journal

journal homepage: www.elsevier.com/locate/cej

Phosphorus slags: Structural insights, dissolution behavior, and potential as sustainable supplementary cementitious materials

Yu Zhang [a], Shuai Nie [b,*], Chen Liu [c,*]

[a] Key Laboratory of Concrete and Prestressed Concrete Structures of the Ministry of Education, Southeast University, Nanjing 210096, China
[b] State Key Laboratory of Silicate Materials for Architectures, Wuhan University of Technology, Wuhan 430070, China
[c] Microlab, Section of Materials and Environment, Faculty of Civil Engineering and Geosciences, Delft University of Technology, 2628 CN, Delft, the Netherlands

ARTICLE INFO

Keywords:
Phosphorus slag
Glass network
Pozzolanic reactivity
Hydration products
^{27}Al, ^{29}Si, and ^{31}P MAS NMR

ABSTRACT

Phosphorus slags, abundant industrial by-products, hold significant potential for use as supplementary cementitious materials (SCM). To explore its application, phosphorus slags with varying contents of P_2O_5 were synthesized, and their network structure, dissolution behaviour, and hydration products in cementitious systems were investigated. The results showed that the pozzolanic reactivity initially decreased and then increased with increasing P_2O_5 content from 3.11 to 8.32 wt%. This behaviour was attributed to the competition between silicate network repolymerization and distortion of aluminium polyhedra. Furthermore, the incorporation of phosphorus increased the fractions of Al_V and Al_{VI} in the glass network, which promoted the incongruent dissolution of Al over Si. Thermodynamic simulation predicted the formation of hydroxyapatite, as the main phosphorus-containing hydration product, which was further confirmed by XRD and NMR results, although with low crystallinity. These findings suggested new perspectives on adopting phosphorus slag as a SCM in cement and concrete production.

1. Introduction

Phosphorus slag is a by-product of yellow phosphorus production using an electric furnace [1–3]. It is mainly composed of CaO and SiO_2 (over 85 wt%), with small amounts of Al_2O_3 and MgO, and contains minor amounts of P_2O_5 (typically less than 5.0 wt%) [4]. This composition is similar to that of blast furnace slag but with the addition of P_2O_5, forming a CaO–SiO_2–Al_2O_3–MgO–P_2O_5 system. The melt-quench process of phosphorus slag results in a predominant glassy phase (>90 wt%), indicating its potential reactivity in an alkaline environment [5–9]. Despite the generation of millions of tons of phosphorus slag globally each year, it is primarily used for landfills [4], mainly due to concerns over residual phosphorus [10–12]. Given the increasing annual production of phosphorus slag, its large-scale utilization is urgently needed.

Blast furnace slag and fly ash, both waste or by-products from the steel industry and coal power plants, respectively, have been widely and successfully utilized as supplementary cementitious materials (SCMs) in the cement and concrete industry [13–15]. This approach not only repurposes industrial waste as a valuable resource but also reduces CO_2 emissions in cement and concrete production by partially replacing cement clinker with SCMs. Notably, >800 kg of CO_2 is emitted for every ton of cement produced [16]. These SCMs participate in latent hydraulic or pozzolanic reactions, with the main reactive components being CaO–SiO_2–Al_2O_3 glassy phases, enhancing the performance of blended cement pastes. However, the availability of these SCMs has been perceived as the major limitation in implementing this solution. Coal-fired power plants are being gradually phased out worldwide, and the hydrogen direct reduction of iron ore (HDRI) steelmaking method has been recently proposed. In the Netherlands, scientists have even attempted to use electricity produced from offshore wind turbines to produce steel by direct electrolysis [17,18]. Therefore, the annual production of fly ash and blast furnace slag is foreseeable to decrease in the near future, and new sources of SCMs need to be explored [19].

The main reactive component in blast furnace slag is the glassy phase, where Si and Al are main network formers. Similar to Si and Al, P can also act as a network former in the network structure of glass. Each phosphorus atom is coordinated with four oxygen atoms, forming PO_4 tetrahedra with a P=O bond. This makes the structure of phosphate glass less compact and rigid compared to silicate glass, resulting in poorer chemical durability [20–22]. However, some experimental results validated that the durability of phosphate glass can be improved by the

* Corresponding authors.
E-mail addresses: nieshuai@whut.edu.cn (S. Nie), c.liu-12@tudelft.nl (C. Liu).

https://doi.org/10.1016/j.cej.2025.160463
Received 10 December 2024; Received in revised form 1 February 2025; Accepted 8 February 2025
Available online 10 February 2025

addition of Al_2O_3 (Al_2O_3–P_2O_5), which strengthens the glass network by the formation of P–O–Al bonds [23–25]. Nevertheless, these studies have focused on phosphate glasses with compositions that differ significantly from phosphorus slag. As a result, the conclusions based on phosphate or aluminophosphate glass cannot be adopted directly to understand the role of P in the network structure of aluminosilicate glass.

Phosphorus slag generally exhibits reactivity similar to fly ash, but less than blast furnace slag, which may be primarily ascribed to its lower Al_2O_3 and MgO contents, as reported in [3,26,27]. When mixed with cement and water, phosphorus slag dissolves, consumes portlandite, and releases Ca and Si ions, leading to the formation of additional C-(A-)S-H phases in the cement matrix. Due to its low MgO content, only a small amount of hydrotalcite-like phases can be detected in a cement-phosphorus slag mixture. Moreover, apart from its known effect of delaying cement hydration [3,26], the impact of P_2O_5 on slag dissolution has been largely overlooked. There is limited knowledge about how P_2O_5 affects the reactivity of phosphorus slag and its role in the formation of crystalline hydration products.

To answer these questions, four slags with different P_2O_5 contents (0, 3.11, 5.90, and 8.32 wt%) were synthesized. These three P_2O_5 levels in the synthetic slags represented medium, high, and excessive content found in phosphorus slags, allowing for an assessment of their influence on the structure, dissolution, and pozzolanic reaction in a cementitious environment. The network structure of the anhydrous glassy phases was characterized by X-ray diffraction (XRD), Fourier transform infrared (FTIR) spectroscopy, as well as ^{27}Al, ^{29}Si, and ^{31}P magic angle spinning (MAS) nuclear magnetic resonance (NMR). A hydraulicity (R^3) test on a model cementitious system was then adopted to examine their reactivity. Additionally, a dissolution test in an alkaline solution of pH 13.2 was employed to identify the dissolution characteristics of the synthetic P_2O_5-containing slags under an alkaline environment. Furthermore, thermogravimetric analysis (TGA), XRD, and MAS NMR were performed to characterize the hydration products of synthetic phosphorus slags in cementitious systems. Finally, the influence of P_2O_5 incorporation on the network structure, the pozzolanic reactivity of the calcium aluminosilicate glassy phase, as well as its hydration products were discussed. The results from this study highlight the impact of phosphorus on slag reactivity and its hydration products in cementitious systems, potentially opening new perspectives for the use of phosphorus slags as SCMs.

2. Materials and methodology

2.1. Materials

Four slags, one without phosphorus oxide (P0) and three phosphorus slags (P3, P5, and P8) were synthesized in this work, following the detailed protocols reported in our previous studies [28,29]. Their chemical compositions, prticle size distribution (PSD), specific surface areas (SSA), calculated numbers of non-bridging oxygens (NBO) per network-forming tetrahedra (NBO/T), and R_{Ca+Mg} are listed in Table 1.

The CaO/SiO_2 ratios of the four synthetic slags were maintained at around 1 to ensure consistent basicity across all samples. Moreover, to minimize interference from Al_2O_3 and MgO, their amounts were kept in the range of 14–16 wt% and 7–9 wt%, respectively. The composition of the P0 slag represents the chemical composition of commercial blast furnace slag commonly available on the market and the slag was used as a reference slag. The P_2O_5 contents in the P3, P5, and P8 slags increased from 3.11 to 8.32 wt% (at the proportional expense of CaO and SiO_2), which was slightly higher than the typical P_2O_5 content (~5 wt%) in conventional phosphorus slag. Furthermore, all four synthetic slags exhibited nearly identical particle size distributions (Fig. 1), with a

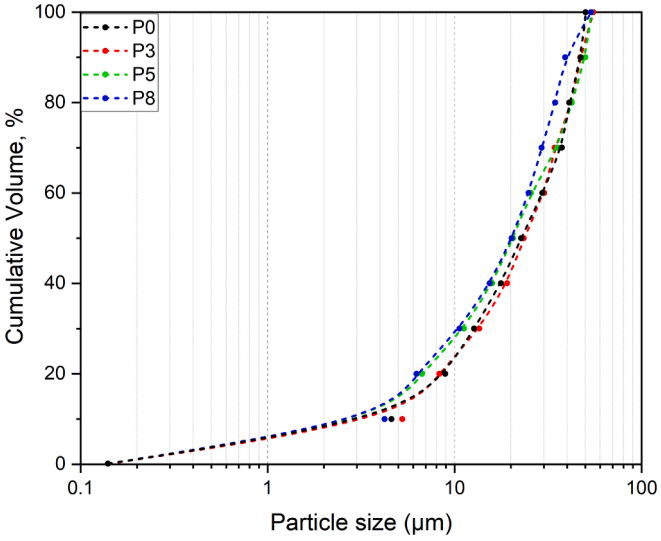

Fig. 1. Particle size distributions of four synthetic slags.

Table 1
Chemical compositions (wt.% and mol.%) determined by XRF analysis and physical properties of synthetic slags.

wt.%					mol.%				
	P0	P3	P5	P8		P0	P3	P5	P8
CaO	37.04	35.43	37.05	33.82	CaO	39.55	39.02	41.15	38.10
SiO_2	37.79	35.89	33.39	31.88	SiO_2	37.72	36.90	34.66	33.57
Al_2O_3	14.51	15.95	13.92	15.42	Al_2O_3	8.52	9.66	8.50	9.55
MgO	8.83	7.75	7.59	9.04	MgO	13.12	11.88	11.73	14.17
P_2O_5	–	3.11	5.90	8.32	P_2O_5	–	1.35	2.59	3.70
Fe_2O_3	0.28	0.25	0.29	0.22	Fe_2O_3	0.10	0.10	0.11	0.09
TiO_2	0.70	0.71	0.91	0.74	TiO_2	0.52	0.55	0.71	0.59
Mn_2O_3	0.17	0.16	0.17	0.16	Mn_2O_3	0.06	0.06	0.07	0.06
Na_2O	0.24	0.28	0.27	–	Na_2O	0.23	0.28	0.27	0.00
K_2O	0.25	0.26	0.27	0.22	K_2O	0.16	0.17	0.18	0.15
SO_3	0.01	0.03	0.04	0.03	SO_3	0.01	0.02	0.03	0.02
[a]d_{50} (μm)	22.73	23.48	20.54	20.25	[c]NBO/T	1.64	1.50	1.75	1.65
[b]SSA (m^2/g)	0.895	0.841	0.946	0.952	[d]R_{Ca+Mg}	2.63	3.11	2.74	3.10

[a]The particle size distribution (PSD) of synthetic slag was measured by EyeTech, Ankersmid.
[b]The specific surface area (SSA) of synthetic slag was measured by nitrogen adsorption with the BET method.
[c]Number of non-bridging oxygens (NBO) per network-forming tetrahedra, NBO/T = (2[Ca] + 2 [Mg] – [Al_{IV}])/([Si] + [Al_{IV}]). Al_{IV} content was determined from the simulation of ^{27} Al MAS NMR spectra using Czjzek model (Table 3).
[d]R_{Ca+Mg} = (Mg + Ca)/2Al, molar ratio. For peraluminous glasses, $R_{Ca+Mg} < 1$ and peralkaline glasses, $R_{Ca+Mg} > 1$.

similar d_{50} value reported in Table 1.

2.2. Characterization of synthetic slag

The synthetic slags were ground and sieved down to <63 μm. A Philips Powder Diffractometer (PW 1830/40) with Cu K-alpha radiation was utilized to collect the XRD pattern and identify the phase present in the anhydrous glasses. Powder samples were scanned in the range of 5°–60° (2θ) with an acceleration voltage of 40 kV, an X-ray beam current of 40 mA, and a step size of 0.03°.

The Fourier transform infrared spectra (FTIR) were obtained through Spectrum TM 100 Optical ATR-FTIR spectrometer, with a wavelength range of 700–1300 cm^{-1}. The measurement adopted a single-beam configuration, and each sample was scanned 20 times with a fixed instrument resolution of 4 cm^{-1}.

The ^{29}Si MAS NMR spectra were acquired at 79.49 MHz on a Bruker Avance 400 NMR (9.4 T) spectrometer with a 4 mm Bruker CP/MAS probe and a spinning frequency (ν_R) of 10 kHz. The single-pulse experiments employed a 45° excitation pulse, a relaxation delay of 30 s, and typically 2000 scans. The ^{29}Si chemical shift was referenced to neat tetramethylsilane (TMS), and larnite (β-C_2S, $\delta(^{29}Si) = -71.33$ ppm) was utilized as a secondary reference. The ^{27}Al MAS NMR were conducted on a Bruker Avance 600 NMR spectrometer using a 4 mm CP/MAS probe with $\nu_R = 13$ kHz, a relaxation delay of 2 s, a short pulse (~15°) and typically 4096 scans. As for the ^{31}P MAS NMR spectra, they were obtained using the similar procedure as the ^{29}Si MAS NMR on Bruker Avance 400 NMR spectrometer, with a relaxation delay of 2 s. Longer relaxation delays were used to ensure that no further increase in spectral intensity occurred, allowing for the acquisition of quantitative NMR spectra. The relatively short relaxation delay observed for the synthetic slags may be ascribed to the presence of a minor amount of iron. The ^{27}Al and ^{31}P chemical shifts were referenced to an aqueous solution of 1.0 M $AlCl_3{\cdot}6H_2O$ and 85 wt% H_3PO_4, respectively.

2.3. Pozzolanic reactivity test

2.3.1. R^3 test

The pozzolanic reactivity of the synthetic phosphorus slag was estimated by the R^3 test, following the mixture of the model system [30–32] containing synthetic slag, portlandite, limestone and KOH and K_2SO_4 solutions, as listed in Table 2. The pH value of the potassium solution (Table 2) was measured to be 12.85, mimicking the alkaline environment of pore solution in blended cement [33]. This model system has proved that its heat evolution presented a good correlation with its compressive strength of SCMs-containing mortar, making it a reliable method for evaluating the pozzolanic reactivity.

The heat evolution during the reaction was measured using a TAM Air isothermal calorimeter at 40 °C over 7 days. In addition, the model paste of each mixture was cast in a 20 mL plastic bottle and cured at 40 °C for 7 and 28 days, respectively, for further tests.

After 7 days of curing, specimens were demoulded, sliced, and then placed in isopropanol to stop hydration. The slices were subsequently ground and manually sieved to obtain a fine powder (<63 μm). For the TGA measurement, approx. 50 mg of the sample powder was heated up from 40 °C to 900 °C with a heating rate of 10 °C/min under an argon atmosphere using a Netzsch STA 449 F3 Jupiter. The bound water content (BW) of each mixture was calculated using the following formula:

Table 2
Mix proportion of the model system for the R^3 test.

	slag	Portlandite	Limestone	Potassium solution [a]
Model system	10.0 g	30.0 g	5.0 g	54 mL

[a] Potassium solution was prepared by dissolving 4.0 g KOH and 20.0 g K_2SO_4 in 1.0 L of deionized water at 20 ± 3 °C.

$$BW = \left(W_{50} - W_{550} - W_{H_2O,CH}\right)/W_{550}$$

Here, W_{50} is the sample weight at 50 °C, W_{550} is the sample weight at 550 °C, and $W_{H_2O,CH}$ is the mass loss from the decomposition of portlandite using the tangent method [34].

2.3.2. Dissolution test

The dissolution test was conducted to monitor the release of elements from synthetic phosphorus slags under an alkaline environment, using a high liquid-to-solid ratio of 1000 to prevent potential precipitation. The effect of P_2O_5 addition on the dissolution characteristics of Ca, Si, Al, and Mg was investigated. In the dissolution test, 1 g of anhydrous slag powder was dissolved in 1000 mL NaOH solution in a sealed polyethylene (PE) bottle at 20 ± 2 °C, following the protocols in [35]. The NaOH solution was prepared by dissolving 5.6 g of NaOH pellets (Sigma-Aldrich) in 1000 mL deionized water. The measured pH value of the prepared NaOH solution was ~13.20, which was comparable to the alkalinity of pore solutions in blended cement systems [33]. Additionally, effective saturation indices (ESI), based on the measured ion concentrations, were calculated to assess which solid phases could form or dissolve from a thermodynamic prospective [36,37]. This approach facilitated the identification of potential hydration products of the synthetic P_2O_5-containing slags.

During the experiment, ~10 mL solution was taken from the PE bottle at each sampling age (1, 2, 4, 6, 8, 24, 48 and 72 h), and the same amount of NaOH solution was added back to keep a constant volume. Subsequently, the extracted solution was filtered and stored in a fridge at 4 °C for further tests. Inductively coupled plasma-optical emission spectroscopy (ICP-OES) with a matrix-matched standard, was utilized to determine the concentrations of Ca, Si, Al, and Mg in solution. The concentration of PO_4^{3-} was measured by ion chromatography (IC), as phosphate (PO_4^{3-}) is the only stable form of phosphorus in high-alkaline conditions [38]. Both ICP-OES and IC spectrometers had a detection limit of 0.1 mg/L. Moreover, the pH of the bulk solution was monitored throughout the dissolution test, and the values were found to be ~13.0 for up to 7 days.

At the same time, thermodynamic modeling was carried out to calculate the effective saturation indices of potential precipitations, using the Gibbs free energy minimization software GEM-Selektor [39] with thermodynamic data from the PSI-GEMS database [40] supplemented by cement-specific data [37,41]. For the possible formation of phosphate-containing phases, *e.g.*, hydroxyapatite ($Ca_5(PO_4)_3(OH)$), bobierrite ($Mg_3(PO_4)_2{\cdot}8H_2O$), and cattiite ($Mg_3(PO_4)_2{\cdot}22H_2O$), *etc.*, the database provided by [42,43] was added in the modelling.

2.4. Hydration products of synthetic slags

Model pastes with a curing age of 28 days were prepared to examine the hydration products of synthetic slags in the cementitious system using TGA, XRD, and NMR. The fine powder (<63 μm) samples used for the measurements were obtained following the same procedure mentioned above.

3. Results

3.1. Structure of anhydrous glass

The XRD patterns of the four synthetic slags (Fig. 2) only showed broad humps without any clear crystalline peaks, implying their amorphous structure with short-range order in the glassy phases. The humps for slags with and without phosphorus incorporation were all centered at ~30°, without significant detected shifts, suggesting that the addition of P_2O_5 did not modify the main alumino-silicate network of the CaO-SiO_2-Al_2O_3-MgO glassy phase notably.

The FTIR spectra of synthetic phosphorus slags (Fig. 3) further

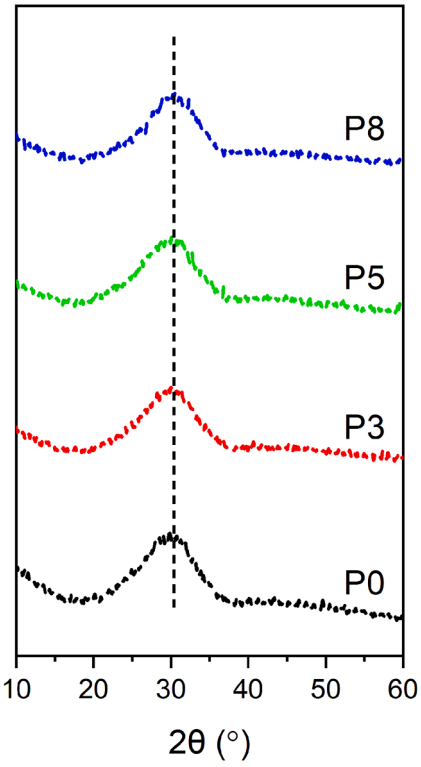

Fig. 2. XRD patterns of the four synthetic phosphorus slags.

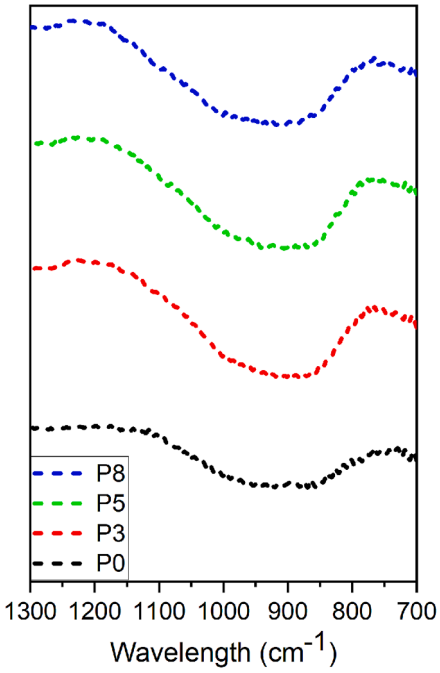

Fig. 3. FTIR spectra for the four synthetic slags with (P3, P5, P8) and without (P0) phosphorus incorporation, the intensity of each spectrum was normalized to its maximum intensity.

supported the amorphous structure of the glassy phase, as reflected by the broad peak between 1300 and 700 cm^{-1}. The broad absorption band from 1100 to 800 cm^{-1} implied the wide existence of different $[SiO_4]^{4-}$ tetrahedral vibration bands, mainly including $[Si_3O_{10}]^{8-}$ (chain, 980–950 cm^{-1}), $[Si_2O_7]^{6-}$ (dimer, 920–900 cm^{-1}) and $[SiO_4]^{4-}$ (monomer, 880–850 cm^{-1}) [44,45]. Overall, it exhibited no clear difference by introducing phosphorus into the system.

As for the absorption of PO bond (P–O and P=O) in the $[PO_4]^{3-}$ tetrahedra, it was also identified in the range of 800–1100 cm^{-1} [46], and modified the vibration state of reference P0 slag. However, it could not be precisely observed due to the strong overlap with Si–O bond in this wavelength range, and thus no quantitative analysis was performed based on this technique.

Due to the lack of long-range order and the intrinsic amorphous network of glassy phase in the synthetic slags, only limited quantitative structure information can be extracted from the XRD patterns and FTIR spectra. ^{27}Al, ^{29}Si, and ^{31}P MAS NMR spectroscopy were employed to provide quantitative and qualitative information on the chemical environments of Si, Al, and P in the alumino-silicate network, complementing the results from XRD and FTIR. ^{29}Si MAS NMR spectra (Fig. 4) for the synthetic anhydrous slags illustrated broad and featureless resonances, located at −90 to −70 ppm, covering the resonances mainly from Q^0, Q^1, Q^2, and Q^3 sites. This observation was consistent with the XRD and FTIR results, and verified the amorphous structure of the glassy phases in these synthetic slags [6,7]. The centre of gravity (δ_{cg}) and full width at half maximum (*FWHM* in short) were utilized to characterize the ^{29}Si resonances, the results are presented in Fig. 5. A noticeable shift of δ_{cg} (^{29}Si) from approx. −75.6 to −79.5 ppm was observed with the incorporation of the lowest amount (3.11 wt%) of phosphorus into slag (from P0 to P3), while no clear shift of δ_{cg} was seen with increasing P_2O_5 content (from P3 to P8). The shifts toward lower frequency suggested the higher polymerization degree of the silicate network structure in the presence of phosphorus. Furthermore, the P-containing slags displayed relatively broad ^{29}Si resonances (*FWHM* of ^{29}Si MAS NMR in Fig. 5) in comparison to the reference P0 slag, implying a more distorted local structure of Si with the addition of P in the network.

The corresponding ^{27}Al MAS NMR spectra exhibited centerband resonances located at ~70 ppm, indicating a predominant presence of Al in tetrahedral coordination [47,48]. This was in accordance with the previous studies on peralkaline ($R_{Ca+Mg}>1$) calcium aluminosilicate glasses [6,7,49]. Besides, indications of the presence of Al_V and Al_{VI} resonances in the ^{27}Al MAS NMR spectra for the slags with higher P_2O_5 contents (P5 and P8) were noted, evidenced by the shoulder and small peak at ~35 and ~15 ppm, respectively.

The contents of Al_{IV}, Al_V, and Al_{VI} sites in these anhydrous slags were quantitatively determined by simulating the centerband lineshapes in the ^{27}Al MAS NMR spectra using the Czjzek model [50]. The results, as illustrated in Table 3, showed that the fractions of Al_V and Al_{VI} increased at the expense of Al_{IV} with increasing phosphorus content in the glassy phase. A clear Al_{VI} site was detected in P8 slag with the highest phosphorus oxide amount (8.32 wt% or 3.70 mol.%). In addition, the distortion of the local environment for the AlO_4 tetrahedra can be revealed by the second-order quadrupolar product parameter, *i.e.*, $P_Q = C_Q(1 + \eta_Q^2/3)^{1/2}$, where C_Q is the quadrupolar interaction constant and η_Q is the asymmetric parameter. The calculated P_Q parameter for Al_{IV} resonances enhanced slightly with the rise of P_2O_5 (Fig. 5), indicating a progressive distortion of the local AlO_4 tetrahedral environment with the incorporation of P in the glass network.

For the ^{31}P MAS NMR spectra (Fig. 4), only one broad featureless resonance centered at ~2 ppm was seen for the P_2O_5-containing slags, which can be assigned to the phosphorus in the form of orthophosphate and/or pyrophosphate [51]. Moreover, the peak intensity was proportional to the P_2O_5 content in the glassy phase, implying that the phosphorus was almost incorporated into the alumino-silicate network without any P_2O_5-containing crystalline phase formation. Note that the ^{31}P δ_{cg} shifted toward a lower frequency with the gradual introduction of P_2O_5 (Fig. 5), whereas the linewidths did not exhibit a systematic trend.

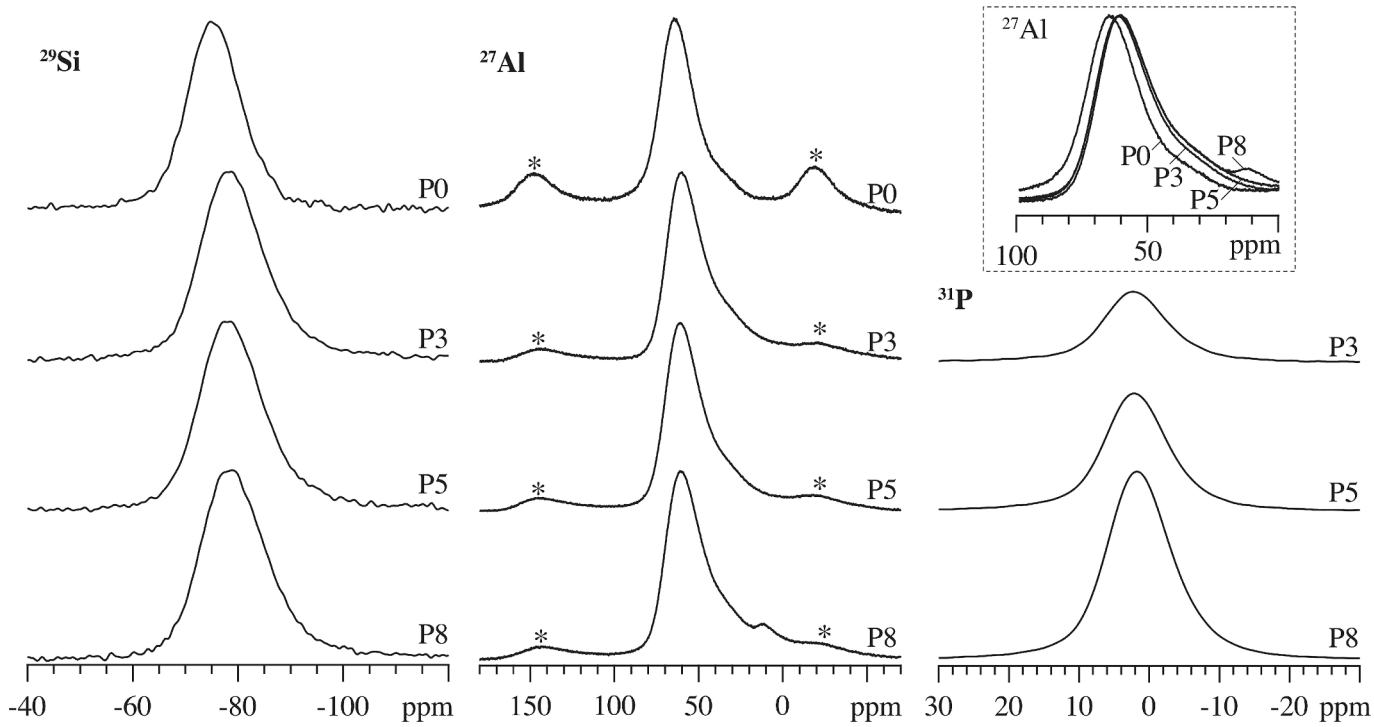

Fig. 4. ^{29}Si (9.4 T), ^{27}Al (14.1 T), and ^{31}P (9.4 T) MAS NMR spectra of the synthetic slags. The asterisks indicate spinning sidebands. The stacked plots of ^{27}Al MAS NMR spectra for the four synthetic slags are shown in the inset.

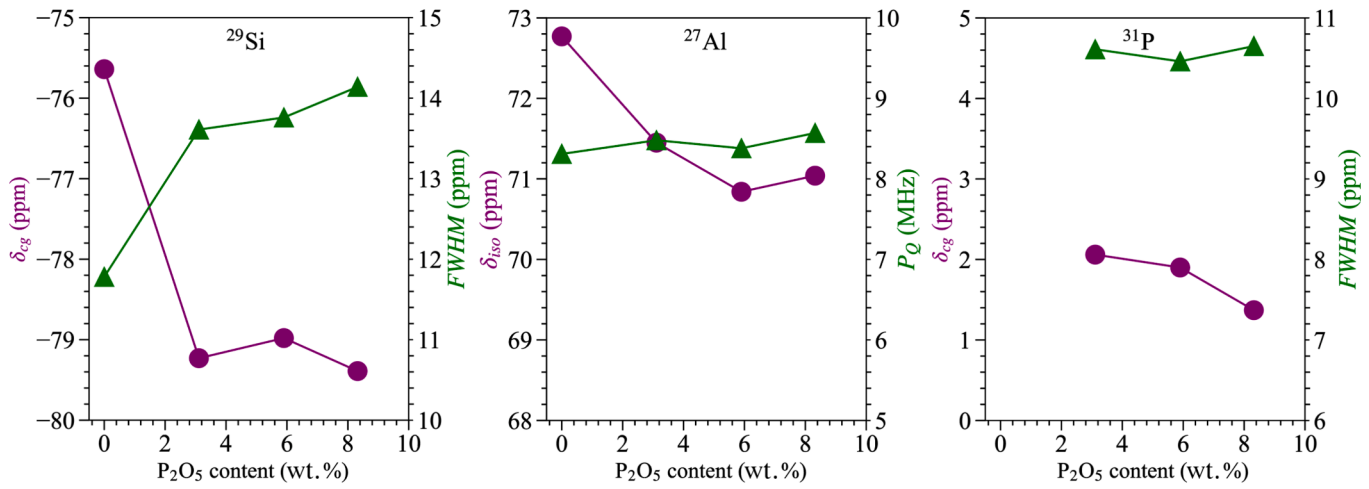

Fig. 5. The ^{27}Al isotropic chemical shifts (δ_{iso}) and quadrupolar product parameters (P_Q) for the Al_{IV} resonances, determined from the satellite transitions [7], as well as the centres of gravity (δ_{cg}) and linewidths (*FWHM*) observed in the ^{29}Si and ^{31}P MAS NMR spectra of the synthesized slags as a function of P_2O_5 content (wt.%). The estimated error limits for δ_{iso}, δ_{cg} and linewidths were ±0.1 ppm, and for P_Q were ±0.1 MHz.

Table 3
Fractions of Al_{IV}, Al_V and Al_{VI} sites determined from simulations of the ^{27}Al MAS NMR spectra using the Czjzek model [50], estimated error limits of which were ± 1 %. The demonstration of the simulation for slag P8 is shown in Fig. A1.

	Al_{IV}	Al_V	Al_{VI}
P0	95.73 %	4.27 %	–
P3	91.34 %	8.66 %	–
P5	88.26 %	11.74 %	–
P8	86.31 %	8.67 %	5.02 %

3.2. Pozzolanic reactivity

3.2.1. R^3 test

3.2.1.1. Heat evolution. Fig. 6 (a) and (b) present the heat evolution rate and cumulative heat release per gram of solid, respectively, as measured by isothermal calorimeter for the four blends with synthetic slags. After contact with water, an initial peak occurred immediately, which can be ascribed to the initial wetting and dissolution of raw materials. Then, the curves were dominated by the main peak within the first day, due to the reaction between synthetic slag and $Ca(OH)_2$. Note that the main peak arose at about 9 h after mixing in the P0 slag blend, and a 3-hour delay of the main peak (located at ~12 h) was observed for the P_2O_5-containing

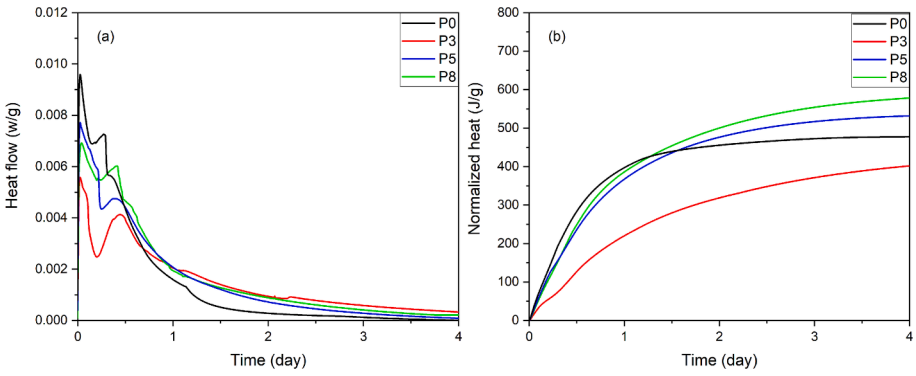

Fig. 6. (a) Heat evolution rate and (b) total heat release as a function of time for blends with synthetic slags at 40 ℃.

slags. The retarding phenomenon can be explained by the following two reasons: (1) phosphorus species released from slag dissolution may react with Ca^{2+} ion, leading to the precipitation of $Ca_{10}(PO_4)_6(OH)_2$. This reduces the Ca^{2+} concentration in the pore solution, thereby delaying hydration products formation, *e.g.*, C-(A-)S-H phase; (2) a decrease in the pH value of the pore solution due to the release of PO_4^{3-} ion, which hinders the further dissolution of slag, as a result. After one day, a distinct hump can be distinguished among slags with and without phosphorus. The heat evolution rate of P0 slag blend decreased to zero quickly after the main peak. Conversely, the deceleration period of phosphorus-containing slags was longer, representing a steady hump. The total heat release increased with increasing phosphorus content in the synthetic slags, as observed in Fig. 6 (b). Compared to P3 slag mixture, ~120 and 170 J/g of additional heat were released in the P5 and P8 systems after 4 days of hydration, respectively. The reference P0 slag blend evolved the most heat before 24 h, and then it was overtaken by the slag P5 and P8 blends. No significant increase in the total heat release for the four synthetic slags was observed from 4 days to 7 days, so this data is not shown in Fig. 6.

3.2.1.2. Bound water content. The chemically bound water contents of the four model blends for the R^3 test after 7 days of hydration are displayed in Fig. 7(a), and their correlation with total heat release is illustrated in Fig. 7(b). The bound water content in each blend generally correlated with the total heat release, which is consistent with the previous studies on similar systems [30,32]. The P_2O_5-containing slags presented higher bound water contents as the P_2O_5 content increased. Lower bound water contents were observed for P3 and P5 blends compared to the reference P0, whereas the P8 blend showed the highest bound water content among the hydrated blends.

3.2.2. Dissolution test

3.2.2.1. Ions concentrations in leachate. The dissolution behaviour of the four synthetic slags has been monitored by dissolving them in NaOH solution with a pH value of ~13.2, and the Ca, Si, and Al concentrations in the solution, normalized to their molar fractions in the raw slags, are present in Fig. 8 (a)–(c). A rapid dissolution was detected for all four synthetic slags up to 10 h, as indicated by the quick increase in Ca, Si, and Al concentrations in the leachate. Subsequently, the release of Ca and Si slowed down for up to 1 day, and the Ca and Si concentrations reached a plateau afterwards. The reduced dissolution rate after 10 h can be attributed to ion accumulation in the leachate, which lowers the undersaturation of the solution, *i.e.*, the main driving force for glassy phase dissolution [35,52,53]. The dissolution of Al in the reference P0 slag displayed a similar trend as Si. For the concentration of phosphate species (PO_4^{3-} in Fig. 9 (d)), no clear trend was observed as a function of dissolution time or P_2O_5 content in the slag, was observed in the solution. It fluctuated within the range of 1.0–2.5 mg/L. Additionally, the Mg concentration was very low, even below the detection limit (0.1 mg/L) at some sampling points, thus it was not shown here.

In comparison with the reference slag P0, the phosphorus slags illustrated higher Si and Al concentrations, and their contents increased with higher P_2O_5 content. This was more pronounced for the dissolution of Al, and its concentration in the leachate for slag P8 was almost 3 times higher than slag P0 after 3 days of dissolution. This explains the steady hump in the decreasing period of calorimetric measurement of phosphorus slags (Fig. 7(a)), where enhanced Al release promoted the

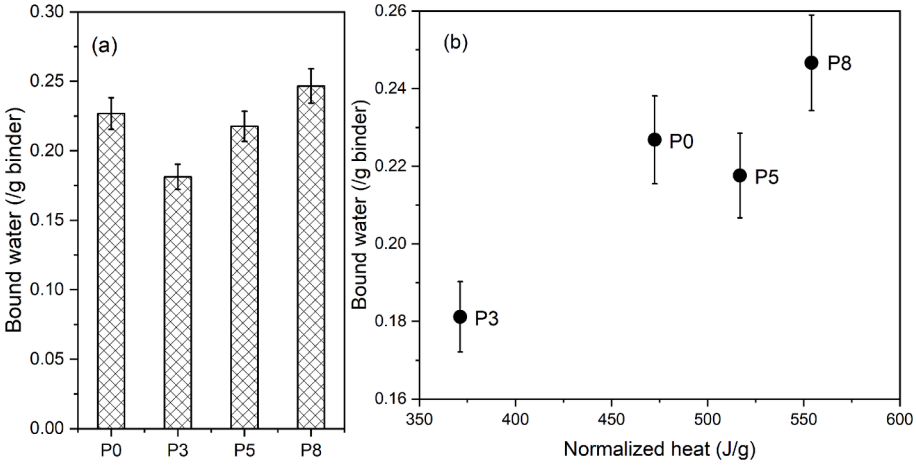

Fig. 7. (a) Chemically bound water content of each model blend after 7 days of curing at 40 °C; (b) correlation between bound water content and cumulative heat release at 7 days.

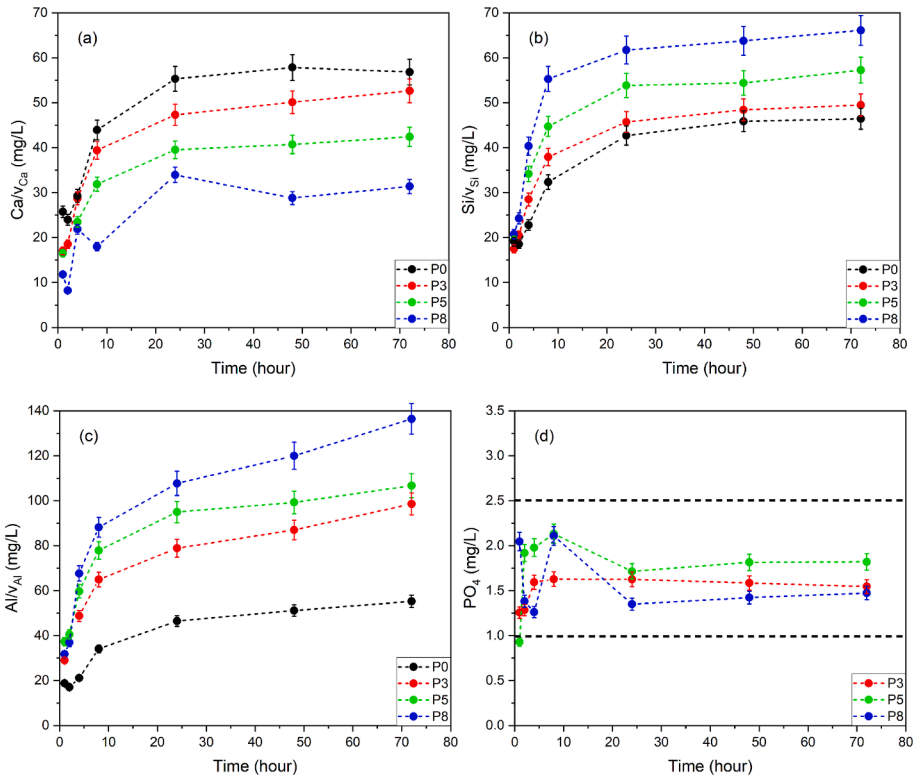

Fig. 8. (a) Ca, (b) Si, and (c) Al concentrations in the leachate normalized to their corresponding molar fractions in raw synthetic slags and plotted as a function of dissolution time up to 3 days; (d) detected PO_4^{3-} concentrations in the solution for the synthetic phosphorus slags.

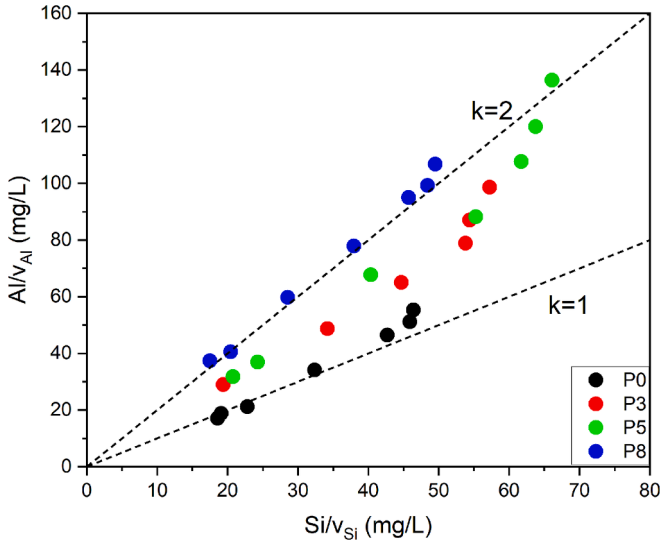

Fig. 9. Correlation between the Al and Si concentrations in the leachate normalized to their molar fractions in raw synthetic slags.

formation of calcium aluminate hydrate phases, *e.g.* ettringite and calcium monocarboaluminate (monocarbonate for short). In contrast, a reduced Ca concentration was found in the solution of phosphorus slags. The more P_2O_5 incorporated in the synthetic slag, the lower Ca concentration observed. This can be ascribed to the precipitation of hydroxyapatite (see the below section of the *Effective saturation index*), consuming Ca ion and delaying the reaction between slag and portlandite (Fig. 7(a)).

The relationship between Al and Si concentrations, normalized to their corresponding molar percentages in the raw slags, is shown in Fig. 9. For the reference P0 slag, a nearly congruent dissolution between Al and Si was observed, indicated by the 1 to 1 linear correlation ($k = 1$ line in Fig. 9), which is consistent with the results studied on the calcium aluminosilicate glasses [35,52,53]. However, incongruent Al and Si dissolution was noticed for all phosphorus slags, as demonstrated by the higher normalized concentration of Al over Si for P3, P5, and P8 slags. Moreover, a normalized Al/Si ratio of ~2.0 ($k = 2$ line in Fig. 9) was found for P8 slag. It implied that the incorporation of P in the calcium aluminosilicate glassy network promoted the preferential release of Al over Si, which will be discussed in detail in Section 4.1.

3.2.2.2. Effective saturation index. The effective saturation index, based on the measured ion concentrations in the leachate, is used to assess whether the target phases will precipitate or dissolve from the thermodynamic point of view [36,37]. A positive value indicates oversaturation with regard to the solid phase, meaning that it can form or precipitate. Conversely, a negative value suggests undersaturation, indicating that the respective solid phase cannot form or will dissolve.

Fig. 10 (a) and (b) show the calculated ESI values of precipitates, including hydrotalcite-like phase, brucite, C-(A-)S-H phase, and hydroxyapatite, for P0 and P5 slags as a function of dissolution time, respectively. Brucite and hydrotalcite-like phases were saturated from the first sampling point (1 h), owing to their low log K_{sp} (solubility product, −11.16 and −51.14 for brucite and hydrotalcite-like phases, respectively) [54]. Hydroxyapatite was also predicted to be oversaturated upon dissolution, although the phosphate content in the solution was low. The precipitation of hydroxyapatite well explained the retarding effect in the reaction between slag and portlandite (Fig. 7 (a)) and the reduced Ca concentration in the solution of P_2O_5-containing slags (Fig. 8 (a)). On the other hand, the calculated ESI values of other phosphate-containing phases (*e.g.*, bobierrite ($Mg_3(PO_4)_2{\cdot}8H_2O$), cattiite ($Mg_3(PO_4)_2{\cdot}22H_2O$),) were far below 0, thus they were not shown. As for the C-(A)-S-H phase, it was below saturation initially; however, this phase became saturated at around 8 and 24 h in the solution of P0 and

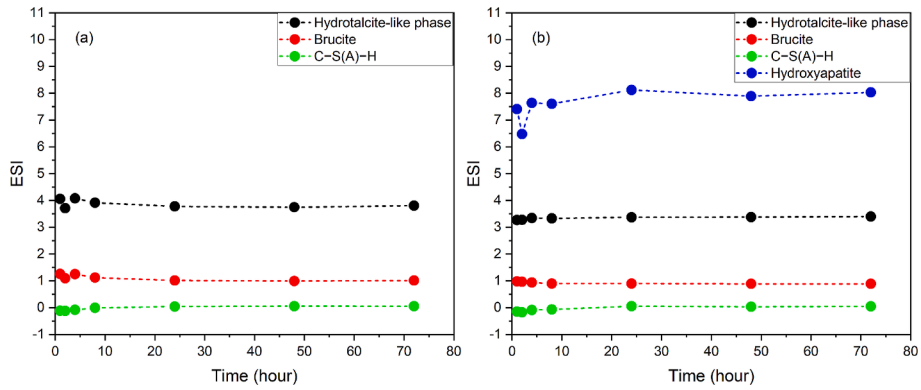

Fig. 10. Calculated effective saturation indices of phases in the solution of slag (a) P0 and (b) P5 as a function of dissolution time. A saturation index of 0.0 indicates an equilibrium state.

P5 slags, respectively. Similarly, due to the formation of hydroxyapatite (competence for Ca), the precipitation of C-(A-)S-H phase in the solution of phosphorus slags was induced.

3.3. Phase assemblage of hydration products

The TG and DTG curves for the four model blends containing synthetic slags after 28 days of curing at 40 °C are displayed in Fig. 11 (a) and (b), respectively. The distinct peak at 400–500 °C can be assigned to the dehydroxylation of $Ca(OH)_2$, and the notable mass loss at 700–800 °C was originated from the decarbonation of limestone. The mass loss for ettringite and C-(A-)S-H phase overlapped at 100 – 150 °C. Besides, because of the presence of $CaCO_3$, monocarbonate (decomposed at ~200 °C) was formed and stabilized ettringite indirectly [55]. In addition, the peak at ~350 °C and the shoulder at ~250 °C suggest the presence of hydrotalcite-like phase, as the hydrate of all synthetic slags.

The X-ray diffraction patterns (Fig. 12) reveal the presence of unreacted portlandite and limestone in the blends for the R^3 test after 28 days of hydration. No clear peak from monosulfate was noticed for all the systems (Fig. 12 (a)). It verified that ettringite was stabilized with the presence of carbonate, consistent with the results of DTG (Fig. 11 (b)). Additionally, monocarbonate was detected instead of hemicarbonate, irrespective of slag composition. It agreed with the results reported in [56], where hemicarbonate was the main carbonate-bearing phase during the first days, but it would eventually transform into monocarbonate at later ages, as monocarbonate was thermodynamically more stable than hemicarbonate. Besides, the monocarbonate content increased continuously with the gradual incorporation of P_2O_5 in slags, and reached maximum in the blend containing P8 slag (Fig. 12 (b)). Indication of the presence of hydroxyapatite was also noticed, illustrated by the hump at ~32° (Fig. 12 (c)) [57,58], and became more obvious in slag P5 and P8 blends. It matched well with the calculated ESI values (Fig. 10 (b)), of which hydroxyapatite was predicted to be oversaturated upon dissolution.

According to the results from XRD and TGA, the phase assemblage for the studied synthetic slag blends used for the R^3 test after 28 days of curing mainly comprised portlandite, ettringite, AFm phases (primarily monocarbonate), hydrotalcite-like phase, hydroxyapatite, and C-(A-)S-H phase. These phases can also be confirmed from the ^{27}Al and ^{31}P MAS NMR spectra (Fig. 13). The difference between ettringite, AFm phases, and hydrotalcite-like phase can be revealed by their distinct resonances from octahedrally coordinated Al in the ^{27}Al MAS NMR spectra, *i.e.*, ettringite $\delta_{iso}(^{27}Al)$ = ~13.4 ppm [59], AFm phases $\delta_{iso}(^{27}Al)$ = 9–11 ppm [60], and hydrotalcite-like phase $\delta_{iso}(^{27}Al)$ = ~10.1 ppm [61]. The resonances of tetrahedrally coordination Al in the C-(A)-S-H phase were located in the range of 50–70 ppm [48]. As for the chemical environment of phosphate in hydroxyapatite, it can be probed by the ^{31}P MAS NMR, *i.e.*, hydroxyapatite $\delta_{iso}(^{31}P)$ = 2.75 ppm [57].

For the ^{27}Al MAS NMR spectra, notably higher resonances from AFm phases were detected for the three phosphorus-containing slags, at the expense of ettringite and octahedrally coordinated Al associated with C-(A-)S-H phase ($Al_{VI(C\text{-}A\text{-}S\text{-}H)}$) compared to the reference P0 slag. This was most pronounced in P8 blends, with the highest amount of AFm phases observed, which was consistent with the results of XRD (Fig. 12 (a)). Only one peak, resonanced at ~3 ppm, was observed in the ^{31}P MAS NMR spectra for the P_2O_5-containing slag blends hydrated for 28 days. The small ^{31}P chemical shift difference between anhydrous glass (~2 ppm) and hydrated phosphorous species (~3 ppm) implied that the phosphorous species in the hydration products were present in a similar environment to that in anhydrous glassy phase, near calcium ions and associated with silicate and aluminate sites [62]. This might suggest that phosphorus in the hydrated blend was likely present in hydroxyapatite (located at 2.75 ppm for the well-crystallized hydroxyapatite) and/or in

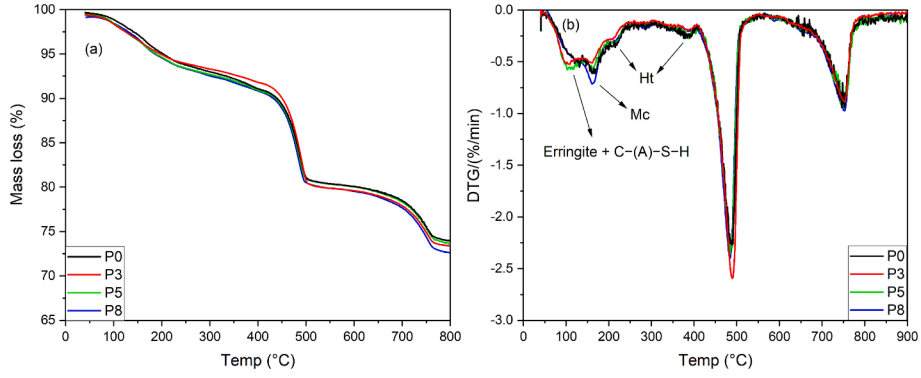

Fig. 11. (a) TG and (b) DTG curves for the four model blends with synthetic slags after 28 days of curing at 40 °C. Mc: monocarbonate; Ht: hydrotalcite-like phase.

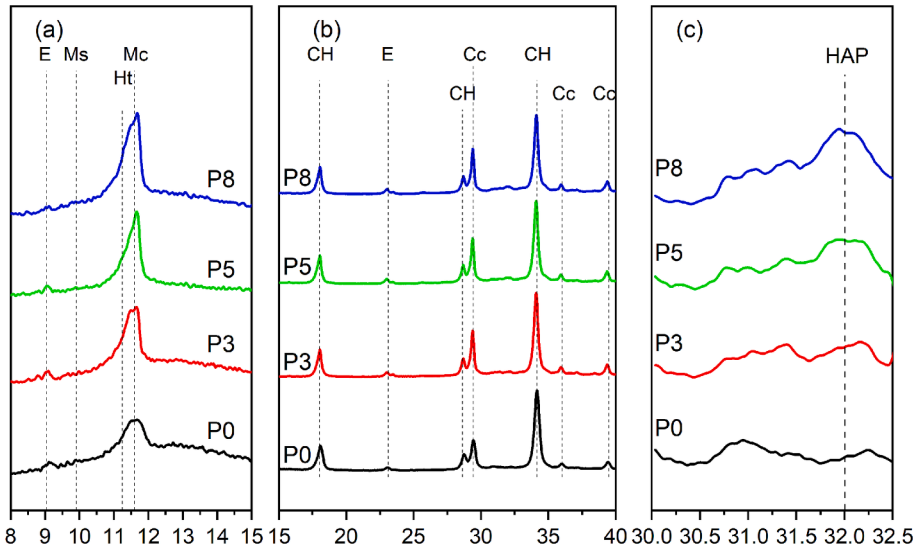

Fig. 12. XRD patterns of the model blend with synthetic slags after 28 days of curing at 40 °C. (a) 8–15°; (b) 15–40°; (c) highlight of 30–32.5°. E – ettringite. Ms: monosulfate; Ht: hydrotalcite-like phase; Mc: monocarbonate; CH: portlandite: Cc: calcium carbonate; HAP: hydroxyapatite.

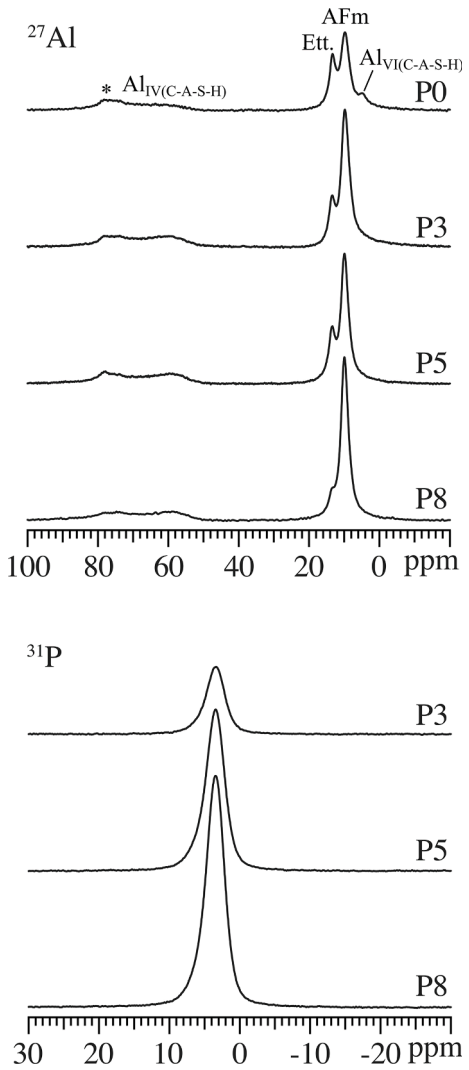

Fig. 13. ^{27}Al (14.1 T) and ^{31}P (9.4 T) MAS NMR spectra for the synthetic slag blends used for the R^3 test after 28 days of hydration. The asterisks indicate spinning sidebands.

the interlayer of C-(A-)S-H phase. Moreover, note that the linewidth (*FWHM*) of the ^{31}P MAS NMR spectra reduced from ~11 ppm to ~3 ppm with hydration, reflecting that the hydrated phosphate units were formed in a more ordered structure. All these results verified the formation of hydroxyapatite in the hydrated blends, complementing the results of XRD measurement (Fig. 12 (c)).

4. Discussion

4.1. Impact of phosphorus on structure and reactivity of calcium aluminosilicate glassy phase

In the network structure of aluminosilicate glass with a composition resembling that of blast furnace slag, SiO_4 and AlO_4 tetrahedra act as the main network formers and construct the amorphous glass framework. Meanwhile, the alkali and alkaline-earth cations play dual roles: they compensate for the negative charges from Al substitution for Si and act as network modifiers, disrupting Si-O-Si bonds within the network structure. For the present investigation, all the studied glassy phases in the synthetic slags were peralkaline glass with $R_{Ca+Mg} = (Mg + Ca)/2Al > 1$, indicating that all AlO_4 tetrahedra were fully charge balanced by Ca and/or Mg. The remaining Ca and Mg cations served as network modifiers, forming NBOs within the amorphous structure and depolymerizing the glass network.

Phosphorus can act as an additional network former in an aluminosilicate glass network. Similar to silicate tetrahedra, each phosphorus atom can also be coordinated with four oxygen atoms and form PO_4 tetrahedra. However, unlike SiO_4 tetrahedra, phosphorus (P^{5+}) in the PO_4 unit has an excess positive charge. As a result, phosphorus forms three single bonds with oxygen atoms, which can act as bridging oxygen connecting to other PO_4/SiO_4/AlO_4 tetrahedra, and one double bond with a fourth oxygen, which remains a non-bridging oxygen. This creates a distinct structural arrangement compared to the SiO_4-AlO_4 network.

In this work, a low phosphorus content, *i.e.*, <5 mol.% (or 8.32 wt%, see Table 1), was introduced into the peralkaline Ca/Mg aluminosilicate glass, resulting in a higher polymerized silicate network, reflected by the chemical shift of ^{29}Si δ_{cg} toward a lower frequency (Fig. 5). This may be attributed to amorphous phase separation caused by the incorporation of phosphorus into the calcium aluminosilicate glass system, leading to the formation of phosphate- and silicate-rich phases. A similar phase separation introduced by phosphorus was observed in the study of a

peralkaline Na_2O–SiO_2–Al_2O_3–MgO–P_2O_5 glass system [63]. The phosphate-rich phase attracted alkali cations to form alkali orthophosphate- and pyrophosphate-like units, reducing the number of alkali cations associated with the silicate network. The removal of these alkali cations associated with silicate tetrahedra, which previously acted as network modifiers, allowed the re-connection of silicate tetrahedra and resulted in a more polymerized silicate network. This agreed well with the results from the studies conducted through both experimental investigations [64] and theoretical calculations using *ab initio* molecular dynamics (AIMD) [65,66]. This repolymerization of the silicate network due to the addition of phosphorus explained the reduced pozzolanic reactivity of P3 slag (3.11 wt%), as indicated by the lower heat release (Fig. 6) and reduced bound water content (Fig. 7) compared to the reference P0 slag. In other words, the reactivity of slag decreased upon a small phosphorus oxide addition, explaining the low reactivity of commercial phosphorus slag with low P_2O_5 content (typically < 3.0 wt%). On the other hand, the silicate network did not exhibit a continuous increase in polymerization with increasing phosphorus content in the glassy phase, as evidenced by the lack of a clear ^{29}Si δ_{cg} shift in Fig. 5.

Compared to the silicate network, phosphorus exerted a more profound impact on the chemical environment of aluminium in the glass. A noticeable ^{27}Al δ_{cg} shift (Fig. 5) occurred as the phosphorus content increased from 3.11 wt% (P3) to 5.90 wt% (P5), with an additional octahedrally coordinated Al site observed in slag P8, containing 8.32 wt % P_2O_5. It suggested that Al was more susceptible to the variation in phosphorus content than Si, and P was preferentially associated with Al, likely through the P-O-Al bonding. The affinity of P with Al in the glass network has also been reported in the AIMD simulation study [66] and the studies [24,25] on enhancing the strength, compactness, and chemical durability of glass via the incorporation of phosphorus. More than double the fraction of Al_V species was detected in the P5 slag compared to the reference P0 slag (Table 3). The increased fraction of reactive Al_V species compensated for the lower reactivity caused by the repolymerization of the silicate network. As a consequence, P5 slag exhibited a similar reactivity to P0 slag. With the further incorporation of P_2O_5 in slag P8, clear Al_{VI} resonance was detected, implying the formation of a more distorted local structure, resulting in its highest reactivity among all the investigated slags.

Following the studies on aluminophosphate glass with the compositions of xAl_2O_3−(50-x)P_2O_5 in the x = 0–10 range [24,25], the results verified that when the molar ratio of P/Al increased, aluminium was mostly located in the Al_V and Al_{VI} units. Although the phosphorus content in the synthetic glassy phases in this work was different, similar results were obtained. With the gradual incorporation of P_2O_5 into the CaO–SiO_2–Al_2O_3–MgO glass network, *i.e.*, the molar ratio of P/Al increased, although the Al_{IV} unit still constituted the dominating aluminium polyhedra, the proportion of Al_V and Al_{VI} rose.

4.2. Hydration products of synthetic phosphorus slags in cementitious environment

The incorporation of phosphorus into slag modified the calcium aluminosilicate glass network, altering the dissolution behaviour of Ca, Si, and Al profoundly. Additionally, the dissolved phosphate species in the pore solution influenced the phase assemblage of hydration products.

Hydroxyapatite was predicted to form in the bulk solution of dissolution test according to thermodynamic modelling. However, the clear identification of hydroxyapatite in the hydrated model paste through current characterization methods was relatively difficult. For example, the main thermal decomposition peak of hydroxyapatite occurred from 350–400 °C, overlapping with the hydrotalcite-like phase [67]. Fortunately, the hump at ~32° (2θ) in the XRD pattern was considered to be originated from hydroxyapatite (ICSD#81442). Since this hump was too broad to be taken as a well-crystalline peak, the hydroxyapatite formed in the model paste might be present as nano-scale crystals, consistent with the results reported in [57,58]. Furthermore, the ^{31}P MAS NMR spectra only showed one resonance at ~3 ppm for all synthetic phosphorous slag blends after 28 days of curing, close to 2.75 ppm for the well-crystallized hydroxyapatite. Compared to the ^{31}P chemical shifts of other orthophosphates [57], this stable chemical speciation of phosphorus in the hydrated paste was strongly suggested as hydroxyapatite. The calcium consumption by micro- or nano-hydroxyapatite formation led to a reduced Ca concentration in the pore solution, thus a delayed main heat peak was observed in the calorimetry measurement. This hydration delay effect caused by the incorporation of phosphorus was more pronounced in the slags with higher P_2O_5 contents (Fig. 6 (a)). Moreover, the quick precipitation of hydroxyapatite also consumed PO_4^{3-} ions, resulting in a low phosphate concentration with prolonged hydration (Fig. 8 (d)). Minor phosphorus might be present in the interlayer of the C-(A-)S-H phase, as reported in [68,69]; however, no clear evidence was found in this study because of the low phosphorus content in slag and the intrinsic amorphous structure of C-(A-)S-H phase.

Compared to the Si–O–Si bonding, the Al–O–P bonding and Al_V as well as Al_{VI} were more vulnerable to hydrolysis. As a result, Al was dissolved into the solution more readily than Si, and an incongruent dissolution of Al over Si was found in P_2O_5-containing slag (Fig. 9). Due to the enhanced Al release in P_2O_5-containing slag, it promoted the steady hump that occurred in the calorimetric measurement of model phosphorus slag pastes (Fig. 6 (a)) and boosted the formation of monocarbonate (Figs. 12 (a) and 13), suggested by the ^{27}Al MAS NMR spectra.

The results obtained in this study were evidently beneficial for optimizing the reactivity of P_2O_5-containing SCMs, *e.g.*, phosphorus slag, not only by changing properties such as fineness but also by manipulating the composition and network structure. As mentioned, phosphorus slag currently produced exhibites a low P_2O_5 content, which was one of the reasons for its low reactivity according to the results of the present investigation. For the best use of this kind of SCM, slightly increasing the P_2O_5 content can be suggested for the industry. Meanwhile, phosphorus-rich SCMs seem to be quite suitable for alkali-activated systems, where fast setting is an issue. The dormant stage can be postponed by several hours, which can be used for casting, transporting, and placing in practice. In addition, the enhanced Al release and thus Al-bearing phases formation in P_2O_5-containing slag indicated that it is a suitable SCM to interact with limestone, leading to the precipitation of hemi- and mono-carbonate and stabilization of ettringite, improving the early-age strength development of blended cements.

This study mainly focuses on the structural characteristics and dissolution behavior of phosphorus slag as a potential supplementary cementitious material. However, further investigations on its long-term durability, mechanical performance, and other key properties are needed to fully assess the viability of phosphorus and optimize its practical application in construction.

5. Conclusions

The influence of phosphorus on the network structure, pozzolanic reactivity, and hydration products of synthetic slags in cementitious systems was investigated in this study, using XRD, FTIR, and ^{27}Al, ^{29}Si, and ^{31}P MAS NMR. The findings of this study led to the following main conclusions:

- The results determined from the calorimetric measurement and bound water content quantification of the model paste showed that the slag reactivity decreased upon a small P_2O_5 addition. However, it conversely increased with the continuous incorporation of phosphorus, and the highest reactivity was observed in slag with the highest P_2O_5 content.
- In the calcium aluminosilicate glass system, the small introduction of P_2O_5 led to a higher polymerized silicate network and lower glass

reactivity, which may be ascribed to the amorphous phase separation and formation of phosphate- and silicate-rich phases.

- With the further incorporation of P_2O_5, the silicate network did not exhibit further polymerization. Instead, clear Al_V and Al_{VI} resonances were noted, indicating the formation of a more distorted local structure and compensating for the lower glass reactivity caused by the repolymerization of the silicate network.
- Compared to the reference P0 slag, the gradual addition of P_2O_5 in synthetic phosphorus slag modified the phase assemblage of hydrated model paste significantly. On the one hand, nano-hydroxyapatite was confirmed to form in both the bulk solution of dissolution test according to thermodynamic modelling and the hydration products of model paste through XRD and MAS NMR measurements. On the other hand, the formation of Al–O–P bonding and Al_V as well as Al_{VI} promoted the incongruent dissolution of Al over Si in P_2O_5-containing slag. The enhanced Al release boosted the formation of Al-bearing phases in the hydrated cementitious system, *e.g.*, monocarbonate.

CRediT authorship contribution statement

Yu Zhang: Writing – original draft, Software, Methodology, Investigation, Funding acquisition, Formal analysis, Data curation, Conceptualization. **Shuai Nie:** Writing – review & editing, Writing – original draft, Visualization, Validation, Supervision, Software, Resources, Project administration, Methodology, Investigation, Formal analysis, Data curation, Conceptualization. **Chen Liu:** Writing – review & editing, Writing – original draft, Visualization, Validation, Supervision, Software, Project administration, Methodology, Investigation, Formal analysis, Conceptualization.

Declaration of competing interest

The authors declare that they have no known competing financial interests or personal relationships that could have appeared to influence the work reported in this paper.

Acknowledgements

Start-up Research Fund of Southeast University (Grant Number RF1028623287) is gratefully acknowledged for the financial support.

Appendix A

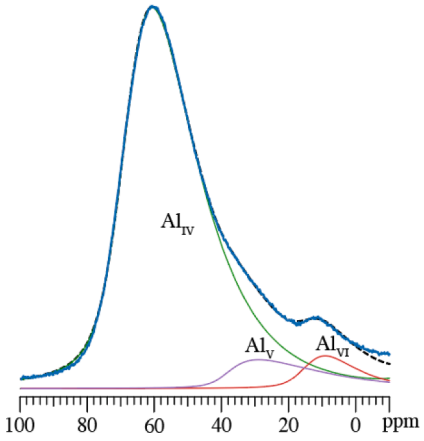

Fig. A1. Simulation of 27Al MAS NMR spectrum of anhydrous P8 slag by using the Czjzek model implemented in ssNake [70].

Data availability

Data will be made available on request.

References

[1] X. Liu, X. Liu, Z. Zhang, Application of yellow phosphorus slag in resource recovery and environmental remediation: a review, J. Environ. Manage. 349 (2024) 119397, https://doi.org/10.1016/j.jenvman.2023.119397.
[2] X. Liu, X. Liu, Z. Zhang, Recycling and comprehensive utilization of yellow phosphorus slag in building materials: a review, Constr. Build. Mater. 396 (2023) 132384, https://doi.org/10.1016/j.conbuildmat.2023.132384.
[3] R. Yang, R. Yu, Z. Shui, X. Gao, X. Xiao, X. Zhang, Y. Wang, Y. He, Low carbon design of an Ultra-High Performance Concrete (UHPC) incorporating phosphorous slag, J. Clean. Prod. 240 (2019) 118157, https://doi.org/10.1016/j.jclepro.2019.118157.
[4] C.L. Yong, K.H. Mo, S. Koting, Phosphorus slag in supplementary cementitious and alkali activated materials: a review on activation methods, Constr. Build. Mater. 352 (2022) 129028, https://doi.org/10.1016/j.conbuildmat.2022.129028.
[5] R.M. Thomsen, S.F. Garzón, D. Herfort, J. Skibsted, Y. Yue, Physical performances of alkali-activated portland cement-glass-limestone blends, J. Am. Ceram. Soc. 100 (2017) 4159–4172, https://doi.org/10.1111/jace.14955.
[6] S. Kucharczyk, M. Zajac, C. Stabler, R.M. Thomsen, M. Ben Haha, J. Skibsted, J. Deja, Structure and reactivity of synthetic CaO-Al_2O_3-SiO_2 glasses, Cem. Concr. Res. 120 (2019) 77–91, https://doi.org/10.1016/j.cemconres.2019.03.004.
[7] S. Nie, R.M. Thomsen, J. Skibsted, Impact of Mg substitution on the structure and pozzolanic reactivity of calcium aluminosilicate (CaO-Al_2O_3-SiO_2) glasses, Cem. Concr. Res. 138 (2020) 106231, https://doi.org/10.1016/j.cemconres.2020.106231.
[8] M. Moesgaard, D. Herfort, M. Steenberg, L.F. Kirkegaard, Y. Yue, Physical performances of blended cements containing calcium aluminosilicate glass powder and limestone, Cem. Concr. Res. 41 (2011) 359–364, https://doi.org/10.1016/j.cemconres.2010.12.005.
[9] M. Moesgaard, S.L. Poulsen, D. Herfort, M. Steenberg, L.F. Kirkegaard, J. Skibsted, Y.Z. Yue, Hydration of blended portland cements containing calcium-aluminosilicate glass powder and limestone, J. Am. Ceram. Soc. 95 (2012) 403–409, https://doi.org/10.1111/j.1551-2916.2011.04902.x.
[10] J.-H. Park, J.J. Wang, S.-H. Kim, J.-S. Cho, S.-W. Kang, R.D. Delaune, D.-C. Seo, Phosphate removal in constructed wetland with rapid cooled basic oxygen furnace slag, Chem. Eng. J. 327 (2017) 713–724, https://doi.org/10.1016/j.cej.2017.06.155.
[11] D. Fang, L. Huang, Z. Fang, Q. Zhang, Q. Shen, Y. Li, X. Xu, F. Ji, Evaluation of porous calcium silicate hydrate derived from carbide slag for removing phosphate from wastewater, Chem. Eng. J. 354 (2018) 1–11, https://doi.org/10.1016/j.cej.2018.08.001.

[12] L. Deng, Z.-Y. Zhang, J. Wang, J. Cui, Y. Zhang, Phosphorus removal by magnesium-based cementitious material: performance and mechanisms, J. Environ. Chem. Eng. 12 (2024) 112172, https://doi.org/10.1016/j.jece.2024.112172.

[13] E. Aprianti, A huge number of artificial waste material can be supplementary cementitious material (SCM) for concrete production–a review part II, J. Clean. Prod. 142 (2017) 4178–4194, https://doi.org/10.1016/j.jclepro.2015.12.115.

[14] M.C.G. Juenger, R. Snellings, S.A. Bernal, Supplementary cementitious materials: new sources, characterization, and performance insights, Cem. Concr. Res. 122 (2019) 257–273, https://doi.org/10.1016/j.cemconres.2019.05.008.

[15] Y. Wang, X. Huang, S. Zhang, W. Ma, J. Li, Utilization of ultrafine solid waste in the sustainable cementitious material for enhanced performance, Constr. Build. Mater. 417 (2024) 135239, https://doi.org/10.1016/j.conbuildmat.2024.135239.

[16] U.N. Environment, K.L. Scrivener, V.M. John, E.M. Gartner, Eco-efficient cements: potential economically viable solutions for a low-CO_2 cement-based materials industry, Cem. Concr. Res. 114 (2018) 2–26, https://doi.org/10.1016/j.cemconres.2018.03.015.

[17] V. Vogl, M. Åhman, L.J. Nilsson, Assessment of hydrogen direct reduction for fossil-free steelmaking, J. Clean. Prod. 203 (2018) 736–745, https://doi.org/10.1016/j.jclepro.2018.08.279.

[18] A. Bhaskar, M. Assadi, H. Nikpey Somehsaraei, Decarbonization of the iron and steel industry with direct reduction of iron ore with green hydrogen, Energies 13 (2020) 758, https://doi.org/10.3390/en13030758.

[19] R. Snellings, P. Suraneni, J. Skibsted, Future and emerging supplementary cementitious materials, Cem. Concr. Res. 171 (2023) 107199, https://doi.org/10.1016/j.cemconres.2023.107199.

[20] U. Hoppe, A structural model for phosphate glasses, J. Non-Cryst. Solids 195 (1996) 138–147, https://doi.org/10.1016/0022-3093(95)00524-2.

[21] R.K. Brow, Nature of alumina in phosphate glass: I, properties of sodium aluminophosphate glass, J. Am. Ceram. Soc. 76 (2005) 913–918, https://doi.org/10.1111/j.1151-2916.1993.tb05315.x.

[22] R.K. Brow, R.J. Kirkpatrick, G.L. Turner, Nature of alumina in phosphate glass: II, structure of sodium alurninophosphate glass, J. Am. Ceram. Soc. 76 (2005) 919–928, https://doi.org/10.1111/j.1151-2916.1993.tb05316.x.

[23] E. Metwalli, R.K. Brow, Modifier effects on the properties and structures of aluminophosphate glasses, J. Non-Cryst. Solids 289 (2001) 113–122, https://doi.org/10.1016/s0022-3093(01)00704-9.

[24] S. Wegner, L. Van Wüllen, G. Tricot, The structure of aluminophosphate glasses revisited: application of modern solid state NMR strategies to determine structural motifs on intermediate length scales, J. Non-Cryst. Solids 354 (2008) 1703–1714, https://doi.org/10.1016/j.jnoncrysol.2007.10.034.

[25] H. Liu, Y. Lu, Y. Qu, H. Lu, Y. Yue, Effect of the content of Al_2O_3 on structure and properties of calcium-phosphate glasses: two experimental case studies, J. Non-Cryst. Solids 450 (2016) 95–102, https://doi.org/10.1016/j.jnoncrysol.2016.07.043.

[26] Y. Peng, J. Zhang, J. Liu, J. Ke, F. Wang, Properties and microstructure of reactive powder concrete having a high content of phosphorous slag powder and silica fume, Constr. Build. Mater. 101 (2015) 482–487, https://doi.org/10.1016/j.conbuildmat.2015.10.046.

[27] Z. Zhang, Q. Wang, J. Yang, Hydration mechanisms of composite binders containing phosphorus slag at different temperatures, Constr. Build. Mater. 147 (2017) 720–732, https://doi.org/10.1016/j.conbuildmat.2017.04.202.

[28] Y. Zhang, S. Zhang, Y. Chen, O. Çopuroğlu, The effect of slag chemistry on the reactivity of synthetic and commercial slags, Constr. Build. Mater. 335 (2022) 127493, https://doi.org/10.1016/j.conbuildmat.2022.127493.

[29] Y. Zhang, Y. Chen, O. Çopuroğlu, Effect of P_2O_5 incorporated in slag on the hydration characteristics of cement-slag system, Constr. Build. Mater. 377 (2023) 131140, https://doi.org/10.1016/j.conbuildmat.2023.131140.

[30] X. Li, R. Snellings, M. Antoni, N.M. Alderete, M. Ben Haha, S. Bishnoi, Ö. Cizer, M. Cyr, K. De Weerdt, Y. Dhandapani, J. Duchesne, J. Haufe, D. Hooton, M. Juenger, S. Kamali-Bernard, S. Kramar, M. Marroccoli, A.M. Joseph, A. Parashar, C. Patapy, J.L. Provis, S. Sabio, M. Santhanam, L. Steger, T. Sui, A. Telesca, A. Vollpracht, F. Vargas, B. Walkley, F. Winnefeld, G. Ye, M. Zajac, S. Zhang, K.L. Scrivener, Reactivity tests for supplementary cementitious materials: RILEM TC 267-TRM phase 1, Mater. Struct. 51 (2018) 151, https://doi.org/10.1617/s11527-018-1269-x.

[31] J. Skibsted, R. Snellings, Reactivity of supplementary cementitious materials (SCMs) in cement blends, Cem. Concr. Res. 124 (2019) 105799, https://doi.org/10.1016/j.cemconres.2019.105799.

[32] R. Snellings, X. Li, F. Avet, K. Scrivener, A rapid, robust, and relevant (R3) reactivity test for supplementary cementitious materials, ACI Mater. J. 116 (2019). https://doi.org/10.14359/51716719.

[33] A. Vollpracht, B. Lothenbach, R. Snellings, J. Haufe, The pore solution of blended cements: a review, Mater. Struct. 49 (2016) 3341–3367, https://doi.org/10.1617/s11527-015-0724-1.

[34] B. Lothenbach, P. Durdzinski, K. De Weerdt, Chapter 5: Thermogravimetric analysis, in: Pract. Guide Microstruct. Anal. Cem. Mater., CRC Press, Boca Raton, 2016: pp. 178–208.

[35] K.C. Newlands, M. Foss, T. Matschei, J. Skibsted, D.E. Macphee, Early stage dissolution characteristics of aluminosilicate glasses with blast furnace slag- and fly-ash-like compositions, J. Am. Ceram. Soc. 100 (2017) 1941–1955, https://doi.org/10.1111/jace.14716.

[36] B. Lothenbach, Thermodynamic equilibrium calculations in cementitious systems, Mater. Struct. 43 (2010) 1413–1433, https://doi.org/10.1617/s11527-010-9592-x.

[37] T. Matschei, B. Lothenbach, F.P. Glasser, Thermodynamic properties of Portland cement hydrates in the system $CaO–Al_2O_3–SiO_2–CaSO_4–CaCO_3–H_2O$, Cem. Concr. Res. 37 (2007) 1379–1410, https://doi.org/10.1016/j.cemconres.2007.06.002.

[38] K.R. Reddy, R.D. DeLaune, P.W. Inglett, Biogeochemistry of Wetlands: Science and Applications, CRC Press, 2022.

[39] D.A. Kulik, T. Wagner, S.V. Dmytrieva, G. Kosakowski, F.F. Hingerl, K. V. Chudnenko, U.R. Berner, GEM-Selektor geochemical modeling package: revised algorithm and GEMS3K numerical kernel for coupled simulation codes, Comput. Geosci. 17 (2013) 1–24, https://doi.org/10.1007/s10596-012-9310-6.

[40] W. Hummel, Nagra/PSI chemical thermodynamic data base 01/01, 35 (2002).

[41] B. Lothenbach, D.A. Kulik, T. Matschei, M. Balonis, L. Baquerizo, B. Dilnesa, G. D. Miron, R.J. Myers, Cemdata 18: a chemical thermodynamic database for hydrated Portland cements and alkali-activated materials, Cem. Concr. Res. 115 (2019) 472–506, https://doi.org/10/ghdgfk.

[42] S. Jebri, I. Khattech, M. Jemal, Standard enthalpy, entropy and Gibbs free energy of formation of A type carbonate phosphocalcium hydroxyapatites, J. Chem. Thermodyn. 106 (2017) 84–94, https://doi.org/10.1016/j.jct.2016.10.035.

[43] B. Lothenbach, B. Xu, F. Winnefeld, Thermodynamic data for magnesium (potassium) phosphates, Appl. Geochem. 111 (2019) 104450, https://doi.org/10.1016/j.apgeochem.2019.104450.

[44] G.-H. Kim, I. Sohn, Effect of Al_2O_3 on the viscosity and structure of calcium silicate-based melts containing Na_2O and CaF_2, J. Non-Cryst. Solids 358 (2012) 1530–1537, https://doi.org/10.1016/j.jnoncrysol.2012.04.009.

[45] S.-M. Han, J.-G. Park, I. Sohn, Surface kinetics of nitrogen dissolution and its correlation to the slag structure in the $CaO-SiO_2$, $CaO-Al_2O_3$, and $CaO-SiO_2-Al_2O_3$ slag system, J. Non-Cryst. Solids 357 (2011) 2868–2875, https://doi.org/10.1016/j.jnoncrysol.2011.03.023.

[46] Y. Sun, Z. Zhang, L. Liu, X. Wang, FTIR, Raman and NMR investigation of $CaO–SiO_2–P_2O_5$ and $CaO–SiO_2–TiO_2–P_2O_5$ glasses, J. Non-Cryst. Solids 420 (2015) 26–33, https://doi.org/10.1016/j.jnoncrysol.2015.04.017.

[47] S. Nie, J. Skibsted, Aluminum distribution in C-(A)-S-H and calcium aluminate hydrate phases of Portland cement – metakaolin – limestone blends studied by ^{27}Al and ^{29}Si NMR spectroscopy, Cem. Concr. Res. 186 (2024) 107664, https://doi.org/10.1016/j.cemconres.2024.107664.

[48] C. Liu, Z. Li, S. Nie, J. Skibsted, G. Ye, Structural evolution of calcium sodium aluminosilicate hydrate (C-(N-)A-S-H) gels induced by water exposure: the impact of Na leaching, Cem. Concr. Res. 178 (2024) 107432, https://doi.org/10.1016/j.cemconres.2024.107432.

[49] A. Hamdan, A. Hajimohammadi, B. Njegic, T. Kim, The changes in the reaction kinetics and phase assemblage of sodium silicate-activated $CaO-MgO-Al_2O_3-SiO_2$ glasses induced by the Al replacement by Mg, Cem. Concr. Res. 166 (2023) 107103, https://doi.org/10.1016/j.cemconres.2023.107103.

[50] J.B. d'Espinose de la Caillerie, C. Fretigny, D. Massiot, MAS NMR spectra of quadrupolar nuclei in disordered solids: The Czjzek model, J Magn Reson 192 (2008) 244–251, https://doi.org/10.1016/j.jmr.2008.03.001.

[51] S.L. Poulsen, H.J. Jakobsen, J. Skibsted, Incorporation of phosphorus guest ions in the calcium silicate phases of portland cement from ^{31}P MAS NMR spectroscopy, Inorg. Chem. 49 (2010) 5522–5529, https://doi.org/10.1021/ic100140j.

[52] R. Snellings, Solution-controlled dissolution of supplementary cementitious material glasses at pH 13: the effect of solution composition on glass dissolution rates, J. Am. Ceram. Soc. 96 (2013) 2467–2475, https://doi.org/10.1111/jace.12480.

[53] R. Snellings, Surface chemistry of calcium aluminosilicate glasses, J. Am. Ceram. Soc. 98 (2015) 303–314, https://doi.org/10.1111/jace.13263.

[54] B. Lothenbach, T. Matschei, G. Möschner, F.P. Glasser, Thermodynamic modelling of the effect of temperature on the hydration and porosity of Portland cement, Cem. Concr. Res. 38 (2008) 1–18, https://doi.org/10.1016/j.cemconres.2007.08.017.

[55] S. Adu-Amankwah, M. Zajac, C. Stabler, B. Lothenbach, L. Black, Influence of limestone on the hydration of ternary slag cements, Cem. Concr. Res. 100 (2017) 96–109, https://doi.org/10.1016/j.cemconres.2017.05.013.

[56] T. Matschei, B. Lothenbach, F.P. Glasser, The role of calcium carbonate in cement hydration, Cem. Concr. Res. 37 (2007) 551–558, https://doi.org/10.1016/j.cemconres.2006.10.013.

[57] S. Zhang, C. Zhang, X. Pang, L. Shi, M. Song, B. Yu, X. Kong, Phase compositions and pore structure of phosphate modified calcium aluminate cement hardened pastes with varied dosages of sodium polyphosphate, Cem. Concr. Res. 184 (2024) 107609, https://doi.org/10.1016/j.cemconres.2024.107609.

[58] N. Pramanik, S. Mohapatra, P. Pramanik, P. Bhargava, Processing and properties of nano-hydroxyapatite(n-hap)/poly(ethylene-co-acrylic acid)(EAA) composite using a phosphonic acid coupling agent for orthopedic applications, J. Am. Ceram. Soc. 90 (2007) 369–375, https://doi.org/10.1111/j.1551-2916.2006.01388.x.

[59] J. Skibsted, M.T. Pedersen, J. Holzinger, Resolution of the Two Aluminum Sites in Ettringite by ^{27}Al MAS and MQMAS NMR at Very High Magnetic Field (22.3 T), J. Phys. Chem. C 121 (2017) 4011–4017. https://doi.org/10/f9shbt.

[60] J. Skibsted, E. Henderson, H.J. Jakobsen, Characterization of calcium aluminate phases in cements by ^{27}Al MAS NMR spectroscopy, Inorg. Chem. 32 (1993) 1013–1027, https://doi.org/10.1021/ic00058a043.

[61] P. Faucon, T. Charpentier, D. Bertrandie, A. Nonat, J. Virlet, J.C. Petit, Characterization of calcium aluminate hydrates and related hydrates of cement pastes by ^{27}Al MQ-MAS NMR, Inorg. Chem. 37 (1998) 3726–3733.

[62] T. Sugama, L. Weber, L.E. Brothers, Sodium-polyphosphate-modified fly ash/calcium aluminate blend cement: durability in wet, harsh geothermal environments, Mater. Lett. 44 (2000) 45–53, https://doi.org/10.1016/s0167-577x(00)00002-1.

[63] S.J. Liu, Y.F. Zhang, W. He, Y.Z. Yue, Transparent phosphosilicate glasses containing crystals formed during cooling of melts, J. Non-Cryst. Solids 357 (2011) 3897–3900, https://doi.org/10.1016/j.jnoncrysol.2011.07.029.
[64] A. Nizamutdinova, T. Uesbeck, T. Grammes, D.S. Brauer, L. Van Wüllen, Structural role of phosphate in metaluminous sodium aluminosilicate glasses as studied by solid state NMR spectroscopy, J. Phys. Chem. B 124 (2020) 2691–2701, https://doi.org/10.1021/acs.jpcb.9b11403.
[65] Y. Zhao, J. Du, X. Cao, C. Zhang, G. Xu, X. Qiao, Y. Liu, S. Peng, G. Han, A modified random network model for P_2O_5 –Na_2O–Al_2O_3–SiO_2 glass studied by molecular dynamics simulations, RSC Adv. 11 (2021) 7025–7036, https://doi.org/10.1039/D0RA10810C.
[66] Y. Qian, B. Song, J. Jin, G.I. Prayogo, K. Utimula, K. Nakano, R. Maezono, K. Hongo, G. Zhao, Ab initio molecular dynamics simulation of structural and elastic properties of SiO_2–P_2O_5–Al_2O_3–Na_2O glass, J. Am. Ceram. Soc. 105 (2022) 6604–6615, https://doi.org/10.1111/jace.18614.
[67] K. Tõnsuaadu, K.A. Gross, L. Plūduma, M. Veiderma, A review on the thermal stability of calcium apatites, J. Therm. Anal. Calorim. 110 (2011) 647–659, https://doi.org/10.1007/s10973-011-1877-y.
[68] V.O. Ozcelik, C.E. White, Nanoscale charge-balancing mechanism in alkali-substituted calcium-silicate-hydrate gels, J. Phys. Chem. Lett. 7 (2016) 5266–5272, https://doi.org/10.1021/acs.jpclett.6b02233.
[69] R. Dupuis, J.S. Dolado, J. Surga, A. Ayuela, Doping as a way to protect silicate chains in calcium silicate hydrates, ACS Sustain. Chem. Eng. 6 (2018) 15015–15021, https://doi.org/10.1021/acssuschemeng.8b03488.
[70] S.G.J. van Meerten, W.M.J. Franssen, A.P.M. Kentgens, ssNake: a cross-platform open-source NMR data processing and fitting application, J. Magn. Reson. 301 (2019) 56–66, https://doi.org/10.1016/j.jmr.2019.02.006.